Performance of a double tilted-Rowland-spectrometer on Arcus

Hans M. Günther[a], P. N. Cheimets[b], R. K. Heilmann[a], R. K. Smith[b], and the Arcus collaboration[1]

[a]Massachusetts Institute of Technology, Cambridge, MA, US
[b]Smithsonian Astrophysical Observatory, 60 Garden St, Cambridge, MA, US

ABSTRACT

Spectroscopy of soft X-rays is an extremely powerful tool to understand the physics of the hot plasma in the universe but in many cases, such as kinematic properties of stellar emission lines or weak absorption features, we have reached the limits of current instrumentation. Critical-angle transmission (CAT) gratings blaze the dispersed spectra into high orders and also offer a high throughput. We present detailed ray-traces for the Arcus mission, which promises an effective area > 0.5 m^2 and resolving power > 2500 in the soft X-rays. The mirror consists of Athena-like silicon pore optics (SPOs) arranged in four petals. Each petal spans an azimuth of about 30 degrees and thus offers a point-spread function that is significantly narrower in one dimension than a full mirror would provide. The four channels are split into two pairs, where each pair has its own optical axis. For each pair, CAT gratings are arranged on a tilted Rowland torus and the two separate tori are positioned to overlap in such a way that the dispersed spectra from both pairs can be imaged onto a common set of CCD detectors, while at the same time keeping the requirement of the spectroscopic focus. Our ray-traces show that a set of 16 CCDs is sufficient to cover both zeroths orders and over 90% of the dispersed signal. We study the impact of misalignment, finite size of components, and spacecraft jitter on the spectral resolution and effective area and prove that the design achieves $R > 4000$ even in the presence of these non-ideal effects.

Keywords: ray-tracing, X-ray optics, critical angle transmission grating, ARCUS, Rowland design

1. INTRODUCTION

X-rays observations offer a window into the hot and energetic universe. For many objects, the insight we can gain from X-ray observations is unique in the sense that no comparable diagnostic is available in other wavelength bands. Due to atmospheric absorption, X-ray observations can only be done outside the Earth's atmosphere. The bulk of the existing X-ray data comes from satellite missions which provide much longer mission lifetimes compared with rocket flights or ballon experiments. Over the past decades, the instrumental capabilities in sensitivity, time resolution and spectral resolving power have improved with almost every new mission. Arguably, the largest and most flexible missions currently in operation are Chandra (one of NASA's great observatories) and XMM-Newton (one of ESA's Horizon 2000 cornerstone missions). Both of them provide imaging using CCDs with an intrinsic energy resolution and high-resolution spectroscopy with gratings. Their unprecedented ability to resolve individual lines in X-ray spectra (and in some cases even to resolve line shapes) has opened entire new fields of study. To give just a few examples from sources in our own galaxy, the He-like triplets in classical T Tauri stars reveal line ratios in their density sensitive He-like triplets that prove that part of their emission is powered by an accretion shock;[1–3] the line profiles observed from hot stars reveal dense, hot clumps in their winds;[4] in the super-soft phase of novae outbursts we can observe how the velocity shift of emission and absorption lines change over the course of a few weeks;[5] and in low-mass X-ray binaries narrow resonant absorption lines can be resolved.[6]

Yet, despite these successes we know that we have barely scratched the surface so far and much more can be learned from observations with even higher spectral resolving power and a larger collecting area. To pick up one

---

Send correspondence to H.M.G.
E-mail: hgunther@mit.edu

UV, X-Ray, and Gamma-Ray Space Instrumentation for Astronomy XX, edited by Oswald H. Siegmund,
Proc. of SPIE Vol. 10397, 103970P · © 2017 SPIE · CCC code: 0277-786X/17/$18 · doi: 10.1117/12.2273011

of the examples above again, only a handful of classical T Tauri stars are bright enough to measure the density in the O VII triplet in < 200 ks, and even in TW Hya, the brightest one, time-resolved observations of the density are infeasible. In this paper, we present ray-tracing results for Arcus, a dedicated soft X-ray high-resolution spectroscopy mission that was accepted for Phase A study as a NASA MIDEX mission in 2017. Arcus will have a much larger effective area A_{eff} and resolving power R than the gratings on Chandra or XMM-Newton.

A general overview of the Arcus mission and its science objectives is given in ref. 7. In this paper, we describe ray-trace simulations with the MARXS code. First, we explain the optical design that is based on two tilted Rowland tori (section 2). Details of the simulations are given in section 3. We use those simulations to optimize the position of the CCD detectors (section 4), derive the nominal effective area and spectral resolving power (section 5), to study the impact that partial shadowing by the spacecraft boom would have (section 6), and to see how misalignment of the gratings impact effective area and resolving power (section 7). We end with a short summary in section 8.

2. OPTICAL DESIGN OF ARCUS

Arcus is designed to use the same silicon (Si) pore optics (SPO) that are developed for ESA's Athena mission.[8,9] These optics are light weight and offer large collecting areas. The focal length is 12 m. SPOs are manufactured in modules each of which contains several shells bonded together. The size of these modules varies with the shell radius, but is typically of order 10 cm on the side. Several of these modules are mounted into a "petal" so that each petal holds mirror shells for some range of mirror radii and azimuth angles. Arcus will have two pairs of petals (and thus four petals in total). There are two optical axes, one for each pair of petals, and the two petals of each pair are mounted diametrically opposed to each other. Figure 1 shows this arrangement.

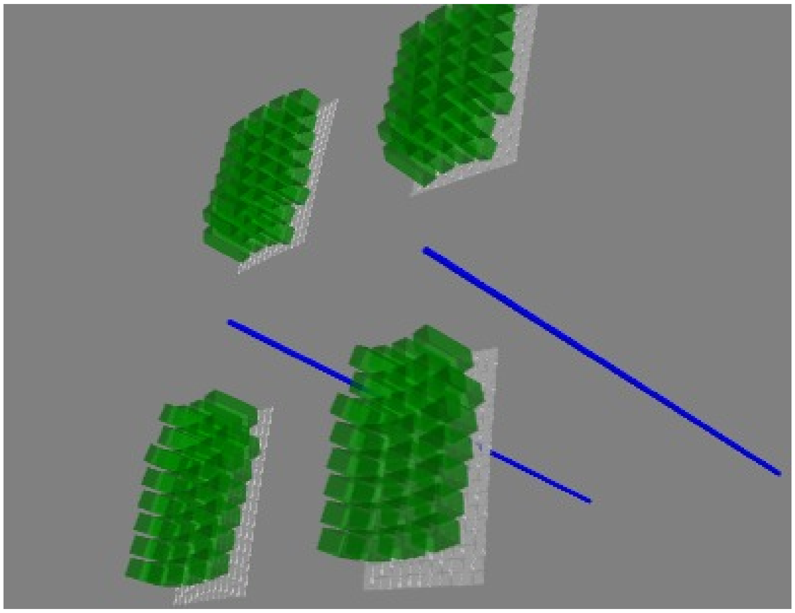

Figure 1. Arcus SPOs (green) are arranged in four petals (support structure of the petals not shown). Two petals each share an optical axis (blue). One preliminary arrangement of CAT gratings is shown in white, this will be optimized in future work.

Critical angle transmission (CAT) gratings[10,11] are located below the SPOs. For each pair of petals, the gratings are arranged on the torus of a Rowland geometry.[12] This torus is tilted[13] such that the center of the Rowland circle is not on either of the optical axes. CAT gratings are most efficient as blazed gratings, i.e. the rays from the SPOs hit the CAT gratings not at normal incidence but rotated by the blaze angle (we chose 1.9 degrees for Arcus) with respect to the normal. For grating facets of finite size, the gratings will always deviate from the curved surface of the Rowland torus at the edges of the grating, and one way to reduce the deviation for blazed gratings is to tilt the Rowland torus.

Blazed CAT gratings concentrate most of the signal into the orders that have a diffraction angle close to twice the blaze angle. Thus, we can catch most of the signal with two sets of CCD detectors: One of them images the zeroth order and the other detectors are centered on twice the blaze angle as measured from the optical axis.

The second pair of petals is shifted with respect to the first one, such that its optical axis coincides with the position of the blaze peak from the first set. Thus, the same CCDs that image the dispersed spectrum of the first set can at the same time image the zeroth order of the second set. By symmetry, the dispersed spectrum from the second set falls in the same region as the zeroth order of the first set. In this way, Arcus makes the most out of a limited number of CCDs. Figure 2 shows a sketch of this setup from two different viewing angles.

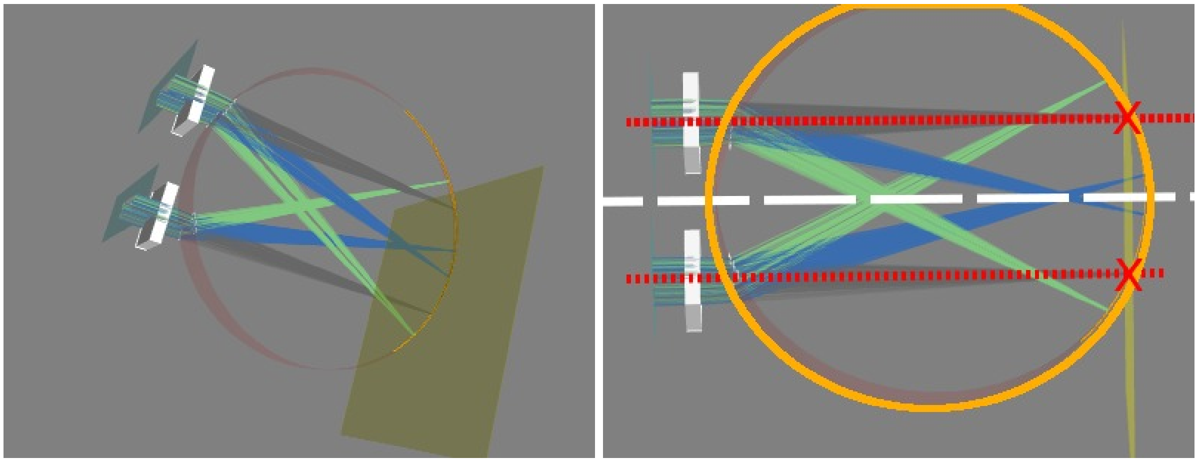

Figure 2. Toy model of the Arcus configuration. Both images show the same rendering from different points of view. The focal length is shortened and the dispersion angle increased compared with the real Arcus to show the conceptual layout. The following components are specifically marked in the right image: The two optical axes (dotted red lines), focal point for each axis (red "x"), Rowland circle (orange), and the plane of symmetry (white dashed line). The two white boxes on the left symbolize one pair of SPO petals for each optical axes. Gray rays indicate zero order photons, which essentially form a cone about each optical axis. We draw a yellow plane through the focal points that is perpendicular to the optical axis. Traditionally, this plane is called "focal plane" (although the focal surface of a Wolter type-I optic is really curved). The focal plane intersects the Rowland circle (orange in the right plot) exactly twice at the locations of the focal points. Blue and green rays indicate dispersed photons. The green rays from the top pair of SPO petals fall close to the zeroth order of the bottom petal and vice versa. Note how the Rowland circle dips below the focal plane between the two focal points.

Data reduction is greatly simplified if the zeroth order from one pair of petals and the dispersed spectrum of the other pair do not overlap on the detector. Thus, one optical axes is offset by +5 mm and the other one by -5 mm compared to the center of a CCD (figure 3). More details on the CCD placement are discussed in section 4.

3. SETUP OF RAY-TRACE SIMULATIONS

Simulations are performed with MARXS version 1.1.[14] MARXS is a python based Monte-Carlo ray-trace code available under an open-source license at `https://github.com/chandra-marx/marxs`. Arcus specific models can be found at `https://github.com/hamogu/arcus`.

In the ray-trace simulations, photons are generated with an energy drawn from a specified spectrum (e.g. for figure 3) or with a fixed energy to build up a grid of energy points e.g. to analyze the spectral resolving power for each energy. All simulations presented in this work assume a source along the nominal pointing direction, but include a random pointing jitter with a Gaussian distribution and a full width at half maximum (FWHM) of 1.86 arcsec.

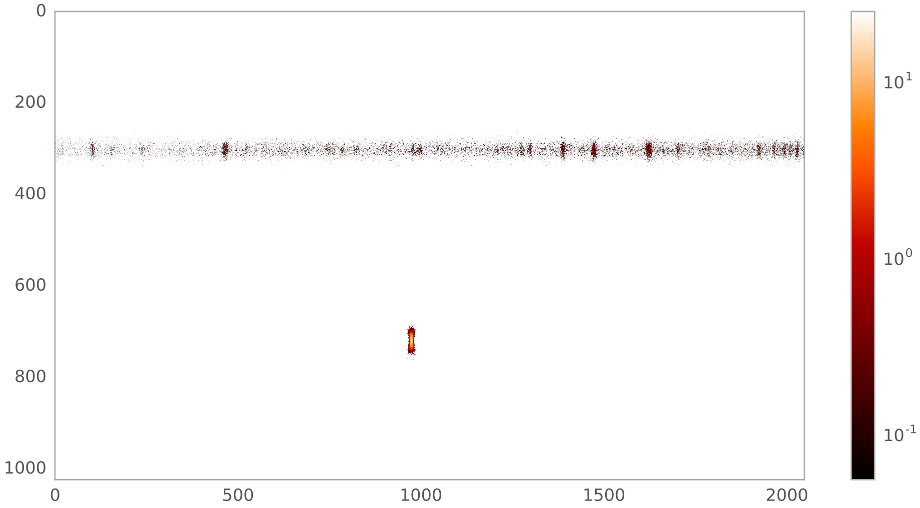

Figure 3. Simulated detector image for a 100 ks observation of the active star EQ Peg. This figure just shows one of the 16 CCDs. On the top is the dispersed spectrum originating from one pair of petals and the associated CAT gratings, at the bottom is the zeroth order image coming from the other pair of petals. Clearly, the offset applied perpendicularly to the dispersion direction is sufficient to separate dispersed spectrum and zeroth order well. X and Y coordinates are given in pixel coordinates. Active stars like EQ Peg have a spectrum that consists of a broad-band continuum and many sharp emission lines. This structure can be seen in the dispersed spectrum on the top. The input spectrum is based on an archival *Chandra* observation. The color scale is logarithmic and represents the expected number of detected events. The simulation does not contain background. Note that the zeroth order has an hour-glass shape typical for sub-apertured mirrors.

The simulations shown here use a simplified mirror model, where all SPOs are described by a single mirror plane. Photons that hit this plane are assigned a new direction in a two-step process. First, they are re-directed by an ideal mirror (i.e. on-axis photons are send to the focal point, but due to the pointing jitter most photons are redirected to some other location in the focal pane close to the focal point), then scattering angles are drawn from a Gaussian distribution in the plane of reflection and out of the plane of reflection. The widths of the scattering distributions are matched to angles observed for SPO proto-types in a beamline.[9,15] This prescription is a good approximation for Wolter type-I optics close to the optical axis, but cannot predict the increase in the size of the point-spread function that occurs several arcminutes away from the optical axis.

The CAT gratings are 30 mm on each side and mounted below the SPOs. In this simulation, they are simply arranged in a regular grid, but their positions can be optimized further in future work to align the structure holding the CAT gratings in place right under the structure holding individual SPO modules. This will reduce the obscuration and increase the effective area by up to a few percent. The grating efficiencies in the simulation are calculated for a dense grid of energies and angles and then scaled to match the efficiencies that are actually measured in the laboratory.[16]

4. POSITIONING THE CCD DETECTORS

As described in section 2, Arcus has two sets of 8 CCD detectors each, where each set covers the zeroth order from one pair of modules and the dispersed spectrum from the other. CCDs are placed tangential to the Rowland torus. The signal in the dispersed spectrum is concentrated at the blaze peak, but some photons are expected at other angles, too. In order to determine the CCD positions that capture the most photons, we run a simulation filling half the Rowland circle with detectors. We then check how many photons are simulated for each CCD and pick the CCDs that capture the most signal.

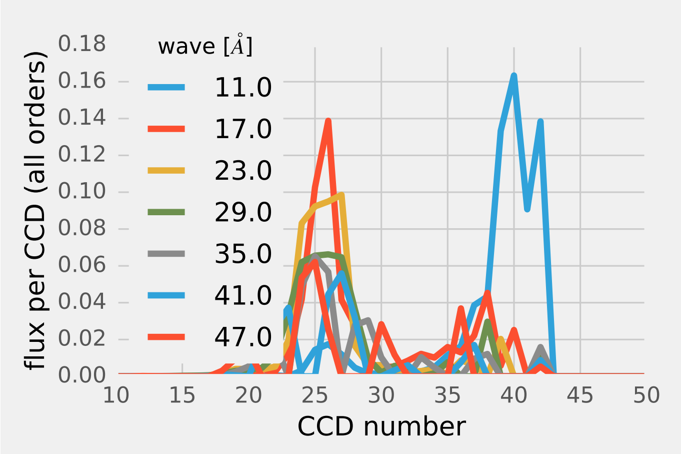

Figure 4. Simulated flux per CCD for simulations with different photon energies using only one pair of petals.

Figure 4 shows the flux per CCD for simulations with different photon energies using one pair of SPO petals only. In this case, the zeroth order is on CCD 40 and most of the photons in a high energy (short wavelength) simulation fall very close to this position because they are not effectively diffracted by the CAT gratings. For longer wavelengths, the CAT gratings do send most of the signal towards the blaze peak. Selecting CCDs with number about 23-30 will catch most of the signal. For the the other pair of SPO petals the dispersed spectrum will be detected in CCD 36-43 and the zeroth order on CCD 24. Consequently, the Arcus design calls for CCDs covering the positions 23-30 and 36-43. The CCD positions of both groups of 8 CCDs are not mirrored exactly with respect to the zero order positions. In this way, we can ensure that a wavelength that falls into a chip gap for one dispersed spectrum will be detected in the other.

CCDs are almost 50 mm long. We repeated the procedure above with an initial CCD arrangement that is shifted by 10, 20, ... mm with respect to the setup used for the simulation in figure 4 but found no significant differences. The blaze peak is a little wider than the area covered by 8 CCDs, so if the CCDs are shifted slightly to one side, a few percent more signal is detected at some wavelengths, but less at others.

5. EFFECTIVE AREA AND RESOLVING POWER

We can now run simulations for a grid of photon energies. MARXS tracks the survival probability for each photon. Each photon starts with a probability of 1 and this number decreases every time the photon interacts with an optical element, e.g. if it reflects off a mirror surface where the probability of absorption is 0.2 and the probability of reflection of 0.8, then this number will be multiplied with 0.8. Thus, we can add up all the probabilities of the detected photons and compare them to the number of initially generated photons. Multiplying this number with the geometrical opening area of the SPOs yields the effective area of the telescope (figure 5).

The second number we derive from these simulations is the spectral resolving power. We define the resolving power R as

$$R = \frac{\lambda}{\Delta\lambda} = \frac{d_x}{FWMH} \tag{1}$$

where λ is the wavelength of the photons, and $\Delta\lambda$ is the observed width of this feature. However, λ and $\Delta\lambda$ are not directly observed by the CCDs. These numbers have to be derived from the position of the detected photons. We project the photon positions from the CCDs onto the focal plane, fit a Gaussian distribution and obtain the distance of the center of the Gaussian from the zeroths order d_x and its FWHM. It occasionally happens that only some fraction of the photons hit a CCD and the rest falls into a chip gap. In this case, the apparent FWHM of the detected photons is smaller than it should be, leading to a spike in the resolving power plotted in figure 6.

We measure R separately for each detected grating order. Higher orders have a higher resolving power because their diffraction angle is larger. For science questions that require the very best resolving power, it would be

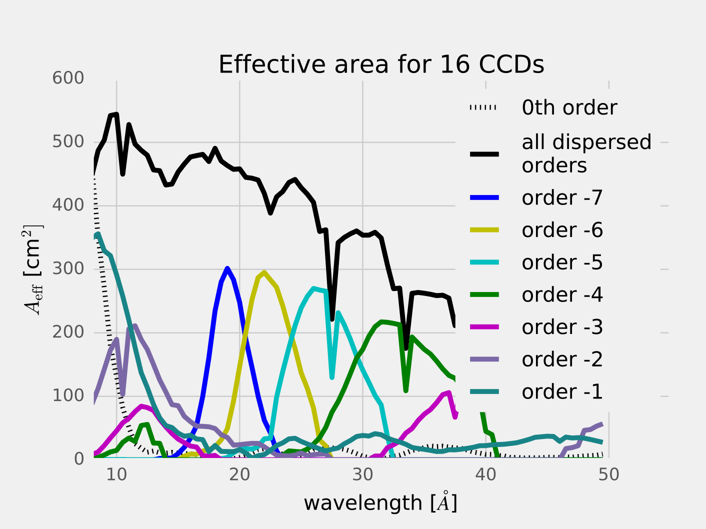

Figure 5. Effective area for Arcus. Notice chip gaps at 28 and 33 Å.

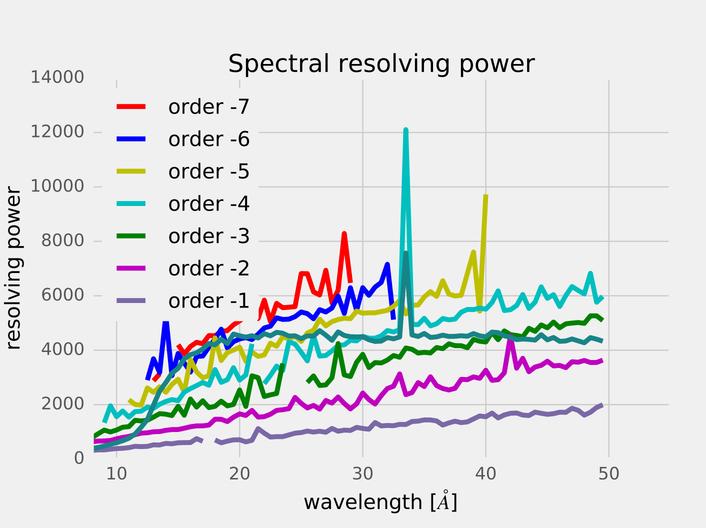

Figure 6. Resolving power for Arcus for a few orders. See text for an explanation or the spurious peak at 34 Å.

possible to analyze only photons in the highest orders. This is sometimes done for *Chandra*/HETG data, where the resolving power in the third order is better than in the first order. On the other hand, the highest detected order might contain only a small fraction of the signal. In figure 7, we average the resolving power for all detected orders, weighting each order by the number of photons it receives.

6. BOOM

The focal lengths of the Arcus SPOs is 12 m, which is more than the size available inside the launch vehicle. Thus, Arcus is planned with an extendible boom which will be extended in orbit. Booms can be manufactured in different sizes and either with a triangular or square cross section. Booms with a smaller circumference are lighter and more commonly used, but on the other hand, the structure of the boom will intercept some of the light. In this section, we simulate the impact that a three-sided boom with different sizes and orientations will have on the effective area. (The resolving power is not affected.) Figure 8 shows one possible set-up of the boom; figure 9 displays a schematic drawing of boom and SPO position. The simulations assume that the material of

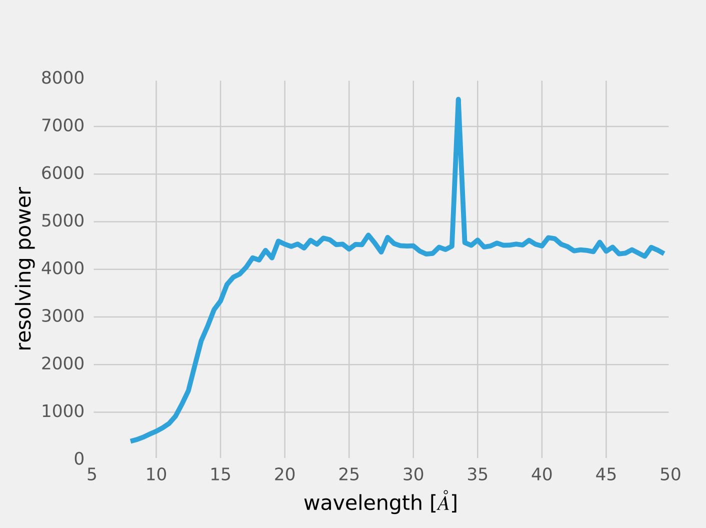

Figure 7. Resolving power for Arcus averaged over all detected orders. See text for an explanation of the spurious peak at 34 Å.

the boom absorbs any photon that intersects the structure and they ignore diffraction on the edges, which is justified because all the elements of the boom are several mm in diameter - much more than the wavelength of X-ray light.

We run simulations for different boom sizes and orientations. The rotation angle of the triangle is a free parameter and can be chosen to minimize the impact. Figure 10 shows the fraction of photons lost due to the boom for the zeroths order and the dispersed orders. Larger boom sizes imply that more of the SPOs are located fully inside the boom and are thus not subject to absorption. For small booms there is a significant angle dependence because for certain angles not only will the light from the SPOs to the center cross through the boom, but some of the CCDs are also outside the boom and will require an additional crossing of the boom structure.

Small booms with only 1.6 m on the side absorb about 15% of the dispersed light but this number drops fast for larger booms (figure 10). A boom that is 2.25 m on each side will block only about 5% of the dispersed light. The impact on the zeroth order is higher, but not important for Arcus. The change in absorption with boom orientation is typically a few %.

Different wavelengths are diffracted to different positions on the CCD array and thus pass through the boom at a different angle, leading to a different probability to hit the boom structure. Figure 11 breaks down the loss of effective are by wavelength for a fixed boom rotation angle. This shows that the short wavelengths are most affected, while only a few percent of the effective area are lost above 15 Å.

Similar calculations can be done for a boom with square footprint. However, a square where each side is only about 1.9 m long would be big enough already to enclose all petals and detectors. A four sided boom might be more challenging to deploy than a three-sided boom, but if a four sided boom is chosen, there is little incentive to make it any smaller than 1.9 m, thus we did not perform simulations for this scenario.

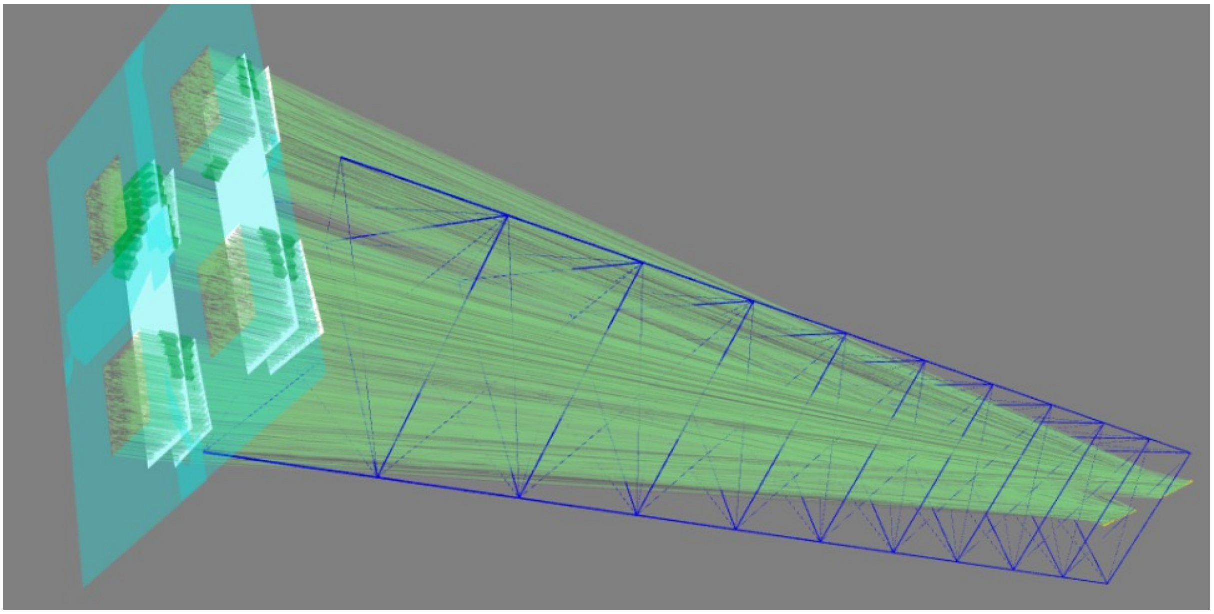

Figure 8. One possible configuration of the Arcus boom. The structure of the boom is shown in blue. The thickness of each element is to scale. Green rays reach the detector, while gray rays hit part of the boom and are absorbed. While each part of the boom is thin, all parts together intercept a measurable fraction of all rays. Photons enter from the left through the openings in the green surface. SPO modules are indicated in green, but in the simplified mirror approximation they are treated as if all reflection happened at a single surface (large white rectangles). CAT gratings are located below the SPOs on the curved surface of the Rowland torus (white elements). CCD detectors are shown in yellow on the right of the figure.

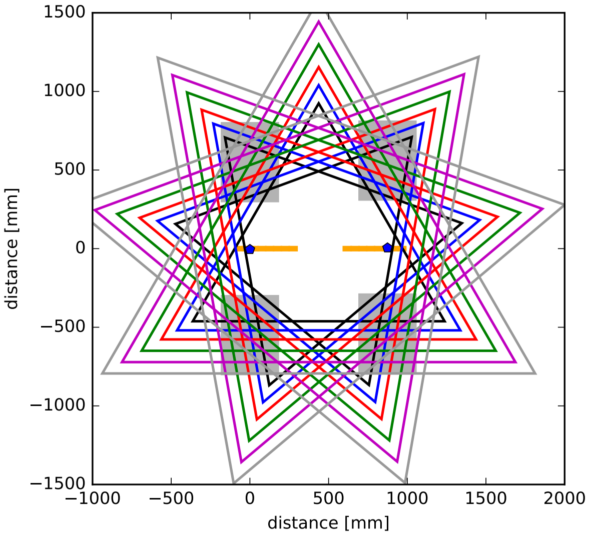

Figure 9. Schematic view of Arcus parallel to the optical axes. Blue pentagons makes the positions of the optical axes. Orange rectangles are CCD detectors (each rectangle consists of eight CCDs; the chip gaps between them are invisible on this scale). Gray rectangles mark the positions of the SPO petals. The colored triangles from black through gray show possible boom sizes. For each size, three different orientations are shown. See figure 10 for a listing of the edge dimension for each triangle.

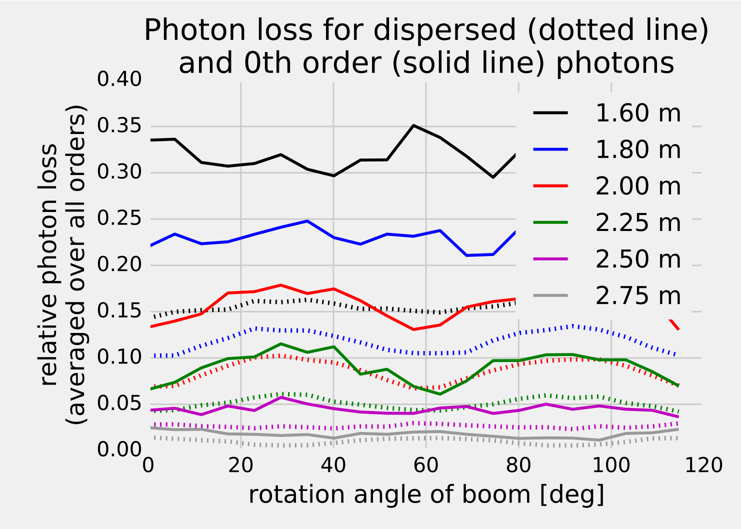

Figure 10. Fraction of photons lost due to boom absorption for a flat input spectrum. See figure 9 for a schematic drawing on the boom positions.

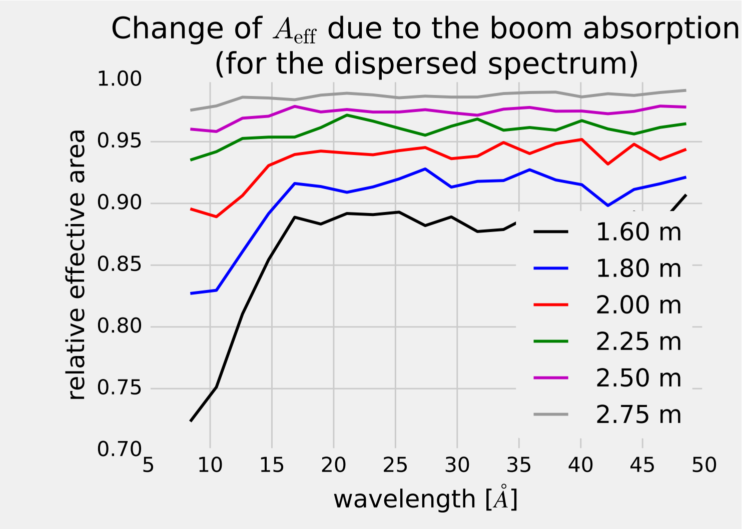

Figure 11. Loss of effective area for different boom sizes.

7. GRATING MISALIGNMENT

Ray-trace simulations are a good tool to analyze the error budget. We can add a random jitter to certain parameters and test how this changes the effective area and resolving power. In this section, we present calculations for grating misalignments. We gave very similar results previously in Ref. 17, which are updated here for the current baseline design of Arcus.

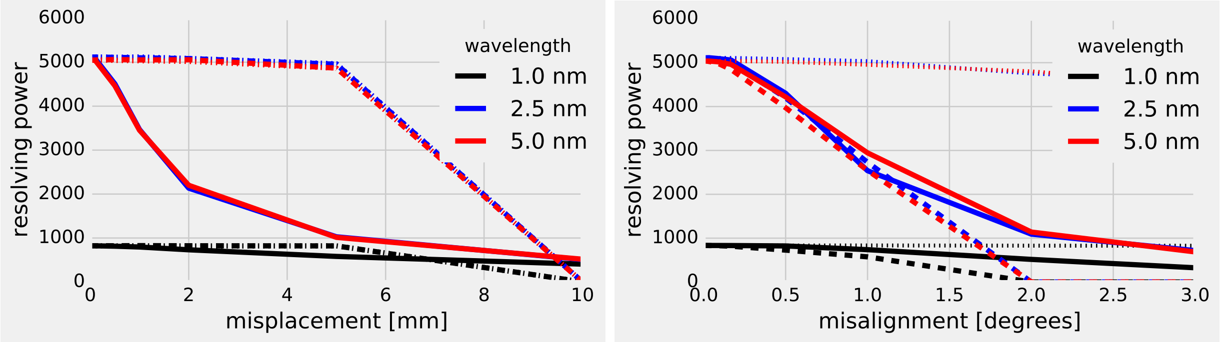

Figure 12. Loss of resolving power due to grating misalignment. Grating coordinates are adjusted by adding a random translation (left) or rotation (right) drawn from a Gaussian distribution of given σ. *solid line*: displacement along (left) or rotation around (right) the grating normal. *dashed line*: Displacement along (left) or rotation around (right) the direction of the grating bars. *dotted line*: Displacement along (left) or rotation around (right) the dispersion direction.

Table 1. Tolerances for facet misalignments to keep the spectral resolving power within 10% of the maximum.

Error source	value
Translation parallel to optical axis	0.5 mm
Translation perpendicular to optical axis	5 mm
Rotation around optical axis	15 arcmin
Rotation around groove direction	15 arcmin
Rotation perpendicular to grooves and optical axes	5 degrees
Stability of grating period	1:a few times 10^5

Figure 12 shows how translation and rotation of the CAT gratings impact the resolving power. Here, we distort the position or rotation of each grating individually along one axis with a value drawn from a Gaussian distribution. Translation of the gratings by about 0.5 mm along the optical axis will reduce the spectral resolving power by about 10%, because the resulting spot on the CCDs is no longer in the spectroscopic focus for most of the rays. On the other hand, moving the gratings by several mm perpendicular to the optical axis has little impact, because this is essentially along the surface of the Rowland torus.

For rotation, the resolving power is reduced by about 10% for a misalignment of order a quarter of a degree around the optical axis or the groove direction. Rotation around the optical axis changes the direction of the dispersed spectrum. Adding up the signal from many stochastically rotated gratings, the signal of a single spectral line on the CCDs will evolve from a spot to a crescent shape. If this effect is large, it could be somewhat be compensated in the data reduction by summing up the signal along a crescent shaped region as opposed to just along a column on the CCD. However, this would be much harder to implement and calibrate. Rotation around the groove direction has a similar impact on the resolving power. Additionally, some effective area is lost because the grating is not illuminated at the most efficient blaze angle any longer and signal is dispersed into lower or higher orders which are not covered by the CCDs. The design is very insensitive to rotation around the last axis and even a misalignment of several degrees does not measurably impact the resolving power. Table 1 summarizes this discussion.

The last point tested here is the change in the resolving power for a random change of the grating period (figure 13). Gratings with different periods will diffract photons by slightly different angles and thus broaden the spot on the CCDs. X-ray measurements on existing CAT gratings indicate that period requirements for Arcus are met with margin.[16, 18]

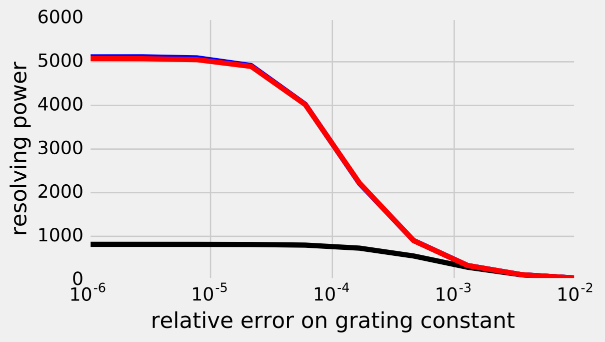

Figure 13. Loss of resolving power for grating period variations.

Similar simulations can be done for misalignment of the SPOs or the CCDs to verify the total error budget, but this beyond the scope of the current paper.

8. SUMMARY

We presented ray-trace calculations for a nominal design for the Arcus mission. From these ray-traces, we derive the effective area and spectral resolving power over the Arcus band-pass. Simulations are done for several possible configurations of a three-sided boom and we calculate the loss of effective area that comes from the obscuration by the boom.

We introduce random translations and rotations to the gratings to determine how accurate the alignment has to be. We find that the most stringent alignment requirement is of order mm for translations and of order of a quarter of a degree for rotations, while requirements are much looser than these numbers along some directions.

ACKNOWLEDGMENTS

Support for this work was provided in part through Smithsonian Astrophysical Observatory (SAO) contract SV3-73016 to MIT for support of the *Chandra* X-Ray Center (CXC), which is operated by SAO for and on behalf of NASA under contract NAS8-03060. The simulations make use of Astropy, a community-developed core Python package for Astronomy,[19] numpy,[20] and IPython.[21]

REFERENCES

[1] Kastner, J. H., Huenemoerder, D. P., Schulz, N. S., Canizares, C. R., and Weintraub, D. A., "Evidence for Accretion: High-Resolution X-Ray Spectroscopy of the Classical T Tauri Star TW Hydrae," *ApJ* **567**, 434–440 (Mar. 2002).

[2] Günther, H. M., Schmitt, J. H. M. M., Robrade, J., and Liefke, C., "X-ray emission from classical T Tauri stars: accretion shocks and coronae?," *A&A* **466**, 1111–1121 (May 2007).

[3] Brickhouse, N. S., Cranmer, S. R., Dupree, A. K., Luna, G. J. M., and Wolk, S., "A Deep Chandra X-Ray Spectrum of the Accreting Young Star TW Hydrae," *ApJ* **710**, 1835–1847 (Feb. 2010).

[4] Schulz, N. S., Canizares, C. R., Huenemoerder, D., and Lee, J. C., "X-Ray Line Emission from the Hot Stellar Wind of θ^1 Orionis C," *ApJ* **545**, L135–L139 (Dec. 2000).

[5] Ness, J.-U., Starrfield, S., Beardmore, A. P., Bode, M. F., Drake, J. J., Evans, A., Gehrz, R. D., Goad, M. R., Gonzalez-Riestra, R., Hauschildt, P., Krautter, J., O'Brien, T. J., Osborne, J. P., Page, K. L., Schönrich, R. A., and Woodward, C. E., "The SSS Phase of RS Ophiuchi Observed with Chandra and XMM-Newton. I. Data and Preliminary Modeling," *ApJ* **665**, 1334–1348 (Aug. 2007).

[6] Sidoli, L., Oosterbroek, T., Parmar, A. N., Lumb, D., and Erd, C., "An XMM-Newton study of the X-ray binary MXB 1659-298 and the discovery of narrow X-ray absorption lines," *A&A* **379**, 540–550 (Nov. 2001).

[7] Smith, Randall, K. and The ARCUS team, "Arcus: Exploring the formation and evolution of clusters, galaxies, and stars."

[8] Collon, M. J., Vacanti, G., Gnther, R., Yanson, A., Barrire, N., Landgraf, B., Vervest, M., Chatbi, A., Beijersbergen, M. W., Bavdaz, M., Wille, E., Haneveld, J., Koelewijn, A., Leenstra, A., Wijnperle, M., van Baren, C., Mller, P., Krumrey, M., Burwitz, V., Pareschi, G., Conconi, P., and Christensen, F. E., "Silicon pore optics development for athena," *Proc. SPIE* **9603**, 96030K–96030K–11 (2015).

[9] Collon, M. J., Ackermann, M., Günther, R., Chatbi, A., Vacanti, G., Vervest, M., Yanson, A., Beijersbergen, M. W., Bavdaz, M., Wille, E., Haneveld, J., Olde Riekerink, M., Koelewijn, A., van Baren, C., Müller, P., Krumrey, M., Burwitz, V., Sironi, G., and Ghigo, M., "Making the athena optics using silicon pore optics," *Proc. SPIE* **9144**, 91442G–91442G–8 (2014).

[10] Heilmann, R. K., Ahn, M., Bruccoleri, A., Chang, C.-H., Gullikson, E. M., Mukherjee, P., and Schattenburg, M. L., "Diffraction efficiency of 200-nm-period critical-angle transmission gratings in the soft x-ray and extreme ultraviolet wavelength bands," *Appl. Opt.* **50**, 1364–1373 (Apr 2011).

[11] Heilmann, R. K., Bruccoleri, A. R., and Schattenburg, M. L., "High-efficiency blazed transmission gratings for high-resolution soft x-ray spectroscopy," *Proc. SPIE* **9603**, 960314–960314–12 (2015).

[12] Beuermann, K. P., Bräuninger, H., and Trümper, J., "Aberrations of a facet-type transmission grating for cosmic x-ray and xuv spectroscopy," *Appl. Opt.* **17**, 2304–2309 (Aug 1978).

[13] Heilmann, R. K., Davis, J. E., Dewey, D., Bautz, M. W., Foster, R., Bruccoleri, A., Mukherjee, P., Robinson, D., Huenemoerder, D. P., Marshall, H. L., Schattenburg, M. L., Schulz, N. S., Guo, L. J., Kaplan, A. F., and Schweikart, R. B., "Critical-angle transmission grating spectrometer for high-resolution soft x-ray spectroscopy on the international x-ray observatory," *Proc. SPIE* **7732**, 77321J–77321J–11 (2010).

[14] Günther, H. M., Frost, J., Sipocz, B., Theriault-Shay, A., and Robitaille, T., "Chandra-marx/marxs: v1.1," (July 2017).

[15] Allured, R. and McEntaffer, R. T., "Analytical alignment tolerances for off-plane reflection grating spectroscopy," *Experimental Astronomy* **36**, 661–677 (Dec. 2013).

[16] Heilmann, R. K., Bruccoleri, A. R., Song, J., Kolodziejczak, J., Gaskin, J. A., O'Dell, S. L., Cheimetz, P., Hertz, E., Smith, R. K., Burwitz, V., Hartner, G., La Caria, M.-M., and Schattenburg, M. L., "Critical-angle transmission grating technology development for high resolving power soft x-ray spectrometers on arcus and lynx," in [*UV, X-Ray, and Gamma-Ray Space Instrumentation for Astronomy XX*], *Proc. SPIE*, paper 10399–39.

[17] Günther, H. M., Bautz, M. W., Heilmann, R. K., Huenemoerder, D. P., Marshall, H. L., Nowak, M. A., and Schulz, N. S., "Ray-tracing critical-angle transmission gratings for the x-ray surveyor and explorer-size missions," *Proc. SPIE* **9905**, 990556–990556–10 (2016).

[18] Heilmann, R. K., Bruccoleri, A. R., Kolodziejczak, J., Gaskin, J. A., O'Dell, S. L., Bhatia, R., and Schattenburg, M. L., "Critical-angle x-ray transmission grating spectrometer with extended bandpass and resolving power $> 10,000$," *Proc. SPIE* **9905**, 99051X–99051X–12 (2016).

[19] Astropy Collaboration, Robitaille, T. P., Tollerud, E. J., Greenfield, P., Droettboom, M., Bray, E., Aldcroft, T., Davis, M., Ginsburg, A., Price-Whelan, A. M., Kerzendorf, W. E., Conley, A., Crighton, N., Barbary, K., Muna, D., Ferguson, H., Grollier, F., Parikh, M. M., Nair, P. H., Günther, H. M., Deil, C., Woillez, J., Conseil, S., Kramer, R., Turner, J. E. H., Singer, L., Fox, R., Weaver, B. A., Zabalza, V., Edwards, Z. I., Azalee Bostroem, K., Burke, D. J., Casey, A. R., Crawford, S. M., Dencheva, N., Ely, J., Jenness, T., Labrie, K., Lim, P. L., Pierfederici, F., Pontzen, A., Ptak, A., Refsdal, B., Servillat, M., and Streicher, O., "Astropy: A community Python package for astronomy," *A&A* **558**, A33 (Oct. 2013).

[20] van der Walt, S., Colbert, S. C., and Varoquaux, G., "The numpy array: A structure for efficient numerical computation," *Computing in Science & Engineering* **13**(2), 22–30 (2011).

[21] Pérez, F. and Granger, B. E., "IPython: a system for interactive scientific computing," *Computing in Science and Engineering* **9**, 21–29 (May 2007).